npj | 2D Materials and Applications

www.nature.com/npj2dmaterials

ARTICLE OPEN

# Large photoelectric-gating effect of two-dimensional van-der-Waals organic/tungsten diselenide heterointerface

Zhi Cai[1], Min Cao[1], Zhepeng Jin[1], Kongyang Yi[1], Xiaosong Chen[1] and Dacheng Wei[1]

Photo- or photoelectric-gating modulation is a promising strategy for high-performance photodetectors, which amplifies photoresponsivity by long-lived trapped charges at the interface. However, the performance is normally limited by the uncontrollable trapping process. Here, we develop a large photoelectric-gating, which enhances interfacial charge trapping process by a van-der-Waals interface with an electric-gating tunable energy barrier in the band alignment. By synergy of photo-gating and electric-gating effects, responsivity and detectivity of 1,4-bis(4-methylstyryl)benzene/tungsten diselenide ($WSe_2$) increase by 25-fold and 3-fold to $3.6 \times 10^6$ A/W and $8.6 \times 10^{14}$ Jones. High-quality two-dimensional van-der-Waals interface is of great importance. Sufficient supply of gas-phase molecules in physical vapor deposition is pivotal to obtain such interface between organic crystal and $WSe_2$. As an application, an electric-gating switchable photodetector has been developed, showing great potential of this strategy not only in high-performance photodetectors but also in new photoelectrical devices.

*npj 2D Materials and Applications* (2018)2:21 ; doi:10.1038/s41699-018-0066-2

## INTRODUCTION

Photo-gating modulation is normally regarded as one of the promising strategies for achieving high-performance photodetection,[1–3] which is realized by introducing another light absorption material to form a heterostructure. The heterostructure probably induces a photovoltaic effect under light irradiation, resulting in long-lived trapped charges at the interface to amplify the photoresponsivity.[4] By this strategy, photodetecting responsivity is greatly improved, especially for two-dimensional (2D) materials. The interfacial charge trapping is of extreme significance for achieving efficient photo-gating modulation; however, until now effectively controlling the trapping process is still lacking, leading to limited success in further increasing the photodetecting responsivity. For instance, 2D transition metal dichalcogenides (TMDs) such as molybdenum disulfide ($MoS_2$) and tungsten diselenide ($WSe_2$) have great potential in various photoelectrical applications,[5–7] owing to their excellent physical,[8,9] optical,[5–7] electrical[10–12] properties as well as advantages such as strong light-matter interaction in a wide range of wavelengths,[13–15] high carrier mobility,[14] thickness-modulated band gap,[16] small dark current compared with graphene, etc. Recently, a photoresponsivity ($R$) (normally $10^3$–$10^4$ A/W, the highest is $1.8 \times 10^5$ A/W) was gained in pristine 2D $WSe_2$ photodetectors.[5,17] Nonetheless, the sensitivity of photodetectors made of pristine 2D TMDs or other 2D materials is limited by the high transmittance of the atomically thin layers.[18] To solve this problem, materials like PbS colloidal quantum dots or other TMDs are introduced. The resulting photo-gating modulation improves the $R$ of $MoS_2$ and $WSe_2$ to $6 \times 10^5$ and $2 \times 10^5$ A/W, respectively.[3,19] However, further increasing the photoresponsivity by normal photo-gating or photoelectric-gating modulation receives limited success, as a result of the absence of accumulated photogenerated carriers at the interface depending on the band alignment.

Organic semiconductors are promising materials for electrical or photoelectrical devices due to their high flexibility, ease of processing,[20] and tunable energy gap ranging from near infrared region to ultraviolet.[21] In the case of organic/TMD heterostructures, Rubrene/$MoS_2$ and C8BTBT/$MoS_2$ only achieve a $R$ of 510 and 22 mA/W, respectively, by photo-gating modulation.[22,23] Currently, the $R$ of organic/TMDs is still lower than 10 A/W. To solve the problem, an effective approach is required to enhance the charge trapping process, thus achieving higher photodetection performance compared with devices under normal photo-gating or photoelectric-gating modulation. Moreover, the van-der-Waals heterointerface quality is also of great importance. As a result of the poor interface quality, impurities in heterostructure interface produced via solution processes usually lead to degradation of device performance.[3,19] Epitaxial growth results in higher interface quality, especially for organic semiconductors. Owing to the ideal epitaxial interface, organic crystal/graphene heterostructures achieve photoresponsivities ($10^4$ A/W) about six orders of magnitude higher than that of pristine graphene.[24] In the case of 2D TMDs, a clear understanding of the epitaxial growth of organic crystals on the surface is still absent, which results in uncontrollable interface quality and low performance of organic/TMDs heterostructures in photoelectrical devices.

Here, we demonstrate a large photoelectric-gating effect, which enhances the interfacial charge trapping process by the synergy of photo-gating and electric-gating effects, leading to higher photoresponsivity compared with devices modulated by normal photo-gating or photoelectrical-gating effect. This strategy requires heterostructures with an interfacial electric-gating tunable energy barrier in the band alignment, which allows unidirectional carrier injection. As an example, wide-band gap 1,4-bis(4-methylstyryl)benzene (p-MSB) crystals are epitaxially grown on 2D $WSe_2$ by physical vapor deposition (PVD). Under photo-gating modulation, the heterostructure exhibits $R$ of 1.4 ×

[1]State Key Laboratory of Molecular Engineering of Polymers, Department of Macromolecular Science, Fudan University, Shanghai 200433, China
Correspondence: Dacheng Wei (weidc@fudan.edu.cn)

Received: 25 February 2018 Revised: 27 May 2018 Accepted: 12 June 2018
Published online: 04 July 2018

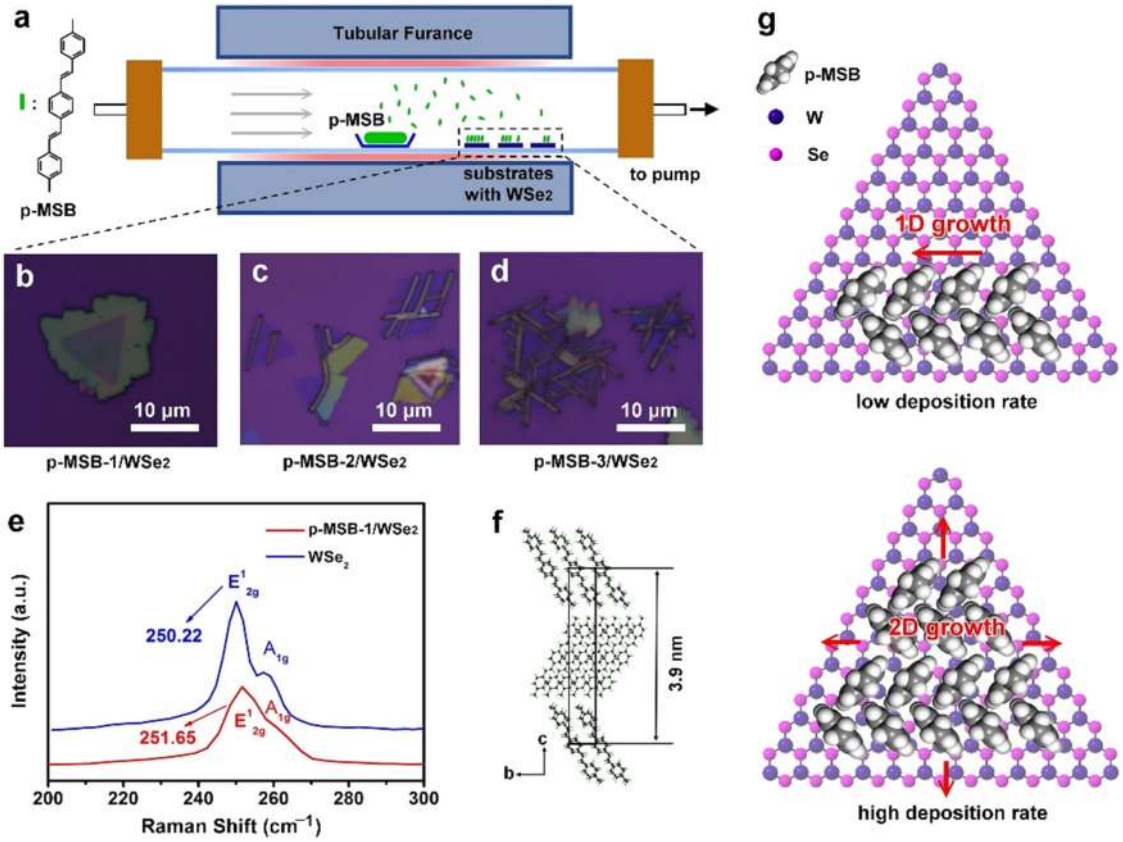


**Fig. 1** Epitaxial growth of p-MSB on $WSe_2$. **a** Schematics of the CVD system. **b–d** Optical microscope images of the p-MSB/$WSe_2$ heterostructures grown on the substrates **b** 12 cm, **c** 13 cm, and **d** 14 cm downstream. **e** Raman spectra of the $WSe_2$ and the p-MSB-1/$WSe_2$. **f** Unit cell structure of p-MSB single crystal with views of the bc plane. **g** One-dimensional (1D) epitaxial growth mode and 2D epitaxial growth mode of p-MSB crystals on $WSe_2$

$10^5$ A/W and detectivity ($D^*$) of $2.5 \times 10^{14}$ Jones (2 μW/cm$^2$ 365 nm light), more than 1 order higher than that of pristine 2D $WSe_2$, respectively. The energy barrier can be tuned higher by electric-gating, thus trapping more photogenerated electrons at the interface. Thus, the resulting gaint photoelectric-gating effect further increases the $R$ and $D^*$ by about 1 order to $3.6 \times 10^6$ A/W and $8.6 \times 10^{14}$ Jones (2 μW/cm$^2$ 365 nm light), 1–9 orders of magnitude higher than that of existing photodetectors based on pristine $WSe_2$[17] or TMDs-based heterostructures, such as PbS/$WSe_2$ ($2 \times 10^5$ A/W),[3] $PPh_3/WSe_2$ ($6.67 \times 10^5$ A/W),[25] graphene/$WSe_2$/graphene (0.01 A/W),[26] $MoS_2/WSe_2$ (0.12 A/W),[27] $MoTe_2$ p–n junction ($5 \times 10^{-3}$ A/W),[28] etc. Moreover, we find that sufficient supply of gas-phase molecules in PVD is the pivotal factor to prepare ideal 2D van-der-Waals interface between organic crystal and TMDs for achieving large photoelectric-gating effect. As an application of the large photoelectrical-gating modulation, we develop an electric-gating switchable photodetector based on p-MSB/$WSe_2$.

## RESULTS

### Epitaxial growth of 2D van-der-Waals p-MSB/$WSe_2$ interface

Triangle 2D $WSe_2$ crystals were produced on $SiO_2$ (300 nm)/Si substrates by chemical vapor deposition (CVD), and then epitaxial growth of p-MSB crystals on $WSe_2$ was conducted by PVD at low pressure (Fig. 1a). The p-MSB molecules were evaporated from the center of the tubular furnace and were deposited on three substrates located 12 cm (p-MSB-1/$WSe_2$), 13 cm (p-MSB-2/$WSe_2$), and 14 cm (p-MSB-3/$WSe_2$) downstream. Figure 1b–d shows optical microscope images of the as-grown samples, which have different morphologies. Most p-MSB-3 crystals have a wire-like structure with growth direction parallel to the edges of triangle $WSe_2$ crystals. Neighbor wires form an angle of 60°, suggesting the epitaxial growth of p-MSB crystals on the $WSe_2$. Most p-MSB-1 crystals have a flake-like structure, covering the whole surface of the $WSe_2$. In the p-MSB-2, both morphologies are observed. Figure 1e shows Raman spectra of $WSe_2$ and p-MSB-1/$WSe_2$. The $WSe_2$ has two characteristic peaks at 250.22 and 257.77 cm$^{-1}$, corresponding to in-plane ($E^1_{2g}$) and out-plane ($A_{1g}$) vibrational modes, respectively.[29] In the case of p-MSB-1/$WSe_2$, these peaks shift to higher wavelength by 1.43 cm$^{-1}$ ($E^1_{2g}$) and 0.73 cm$^{-1}$ in ($A_{1g}$), indicating p-type doping of $WSe_2$ by the p-MSB molecules.[30,31]

The different shapes of as-grown p-MSB crystal grown on $WSe_2$ are attributed to the competition between thermodynamic and kinetic factors (Fig. 1f, g).[32] At low deposition rate, thermodynamic factor dominates. According to Gibbs–Curie–Wulff theorem, the equilibrium shape of a crystal minimizes the total surface energy, thus crystals tended to form wire-like shapes as a result of the strong $\pi$–$\pi$ stacking along (100) direction. Higher concentration of gas-phase molecules is supplied with decreasing the distance. As a result, kinetic factors lead to the extension of every lateral plane regardless of surface free energy difference, forming large flake crystals on the $WSe_2$. Therefore, sufficient supply of the molecules in PVD results in flake p-MSB crystal/$WSe_2$ heterostructures with large-area high-quality 2D van-der-Waals interface. Atomic force microscope (AFM) image (Supplementary Fig. 1) shows that p-MSB molecules are stacked layer-by-layer with a single-layer thickness of 1.75 nm and a plane parallel to the $WSe_2$,[33] indicating the 2D epitaxial growth mode of p-MSB on the $WSe_2$. The p-MSB-1 crystal has a thickness up to 130 nm after 15 min growth. Thus, it has an

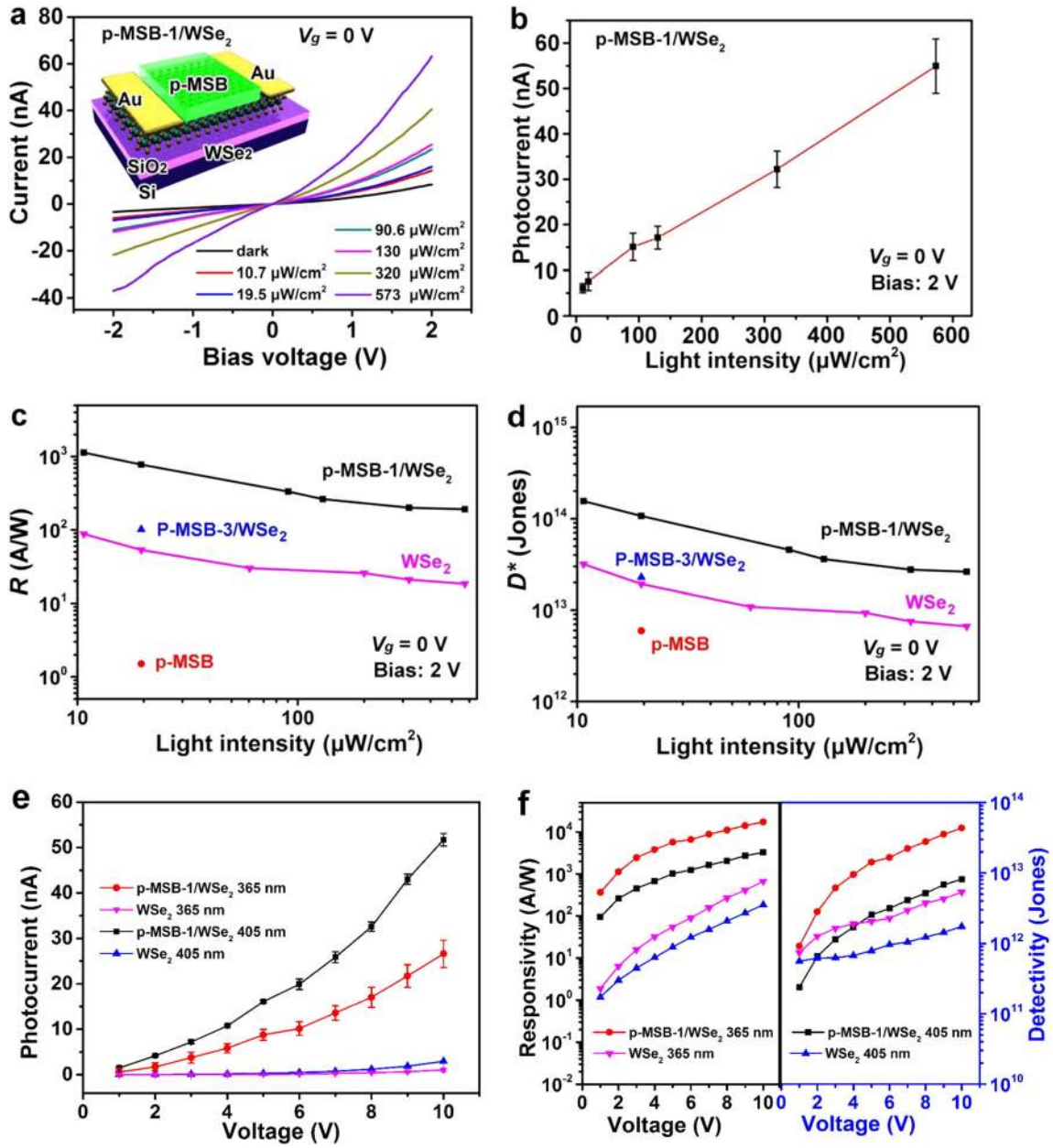


**Fig. 2** Photoresponse under photo-gating modulation (365 nm light, $V_g = 0$ V). **a** Output curves of p-MSB-1/$WSe_2$ under 365 nm incident light with different intensities. The inset is the optical microscope image of the device. **b** Photocurrent (at a 2 V bias) of p-MSB-1/$WSe_2$ under 365 nm incident light with different intensities. **c** The $R$ and **d** the $D^*$ (at a 2 V bias) of p-MSB-1/$WSe_2$, p-MSB-3/$WSe_2$, $WSe_2$, and p-MSB as functions of 365 nm incident light intensity. **e** The photocurrent, **f** $R$ (left) and $D^*$ (right) of p-MSB-1/$WSe_2$ and $WSe_2$ photodetectors under 405 and 365 nm at different bias voltages, the intensity of 365 nm light is 3.6 μW/$cm^2$, and the intensity of 405 nm light is 31.6 μW/$cm^2$

adequate thickness which enables high absorbance of UV light for sensitive photodetection.

## Photoelectrical properties of p-MSB/$WSe_2$

Devices (Fig. 2a, Supplementary Figs. 2–4) were fabricated on p-MSB-1(130 nm thickness)/$WSe_2$, p-MSB-3/$WSe_2$, pristine $WSe_2$ and pristine p-MSB with Au/Cr electrodes, a p++ Si back gate and 300 nm $SiO_2$ as the gate dielectric by electron beam lithography. According to the transfer curves (Supplementary Fig. 5), a positive shift of threshold voltage ($V_{th}$) after p-MSB growth on $WSe_2$ indicates p- type doping effect of the p-MSB molecules.[30,31] The field effect mobilities are calculated up to 72, 57, and $10^{-5}$ $cm^2$/V s for p-MSB-1/$WSe_2$, $WSe_2$, and p-MSB, respectively, indicating high quality of the as-grown samples and the fact that the charge transport mainly takes place in 2D $WSe_2$ instead of the p-MSB crystal. The devices were exposed under 365 or 405 nm UV light irradiation. The output curves (Fig. 2a, Supplementary Fig. 6) of p-MSB-1/$WSe_2$ exhibit remarkably increased current ($I_\lambda$) with light intensity increasing. The photocurrent ($I_{ph} = I_\lambda - I_{dark}$) shows a nearly linear dependence with the light intensity (Fig. 2b, Supplementary Fig. 7), indicating that there are low density of trap states derived from defects of $WSe_2$ and p-MSB.[34,35] Compared with p-MSB-3/$WSe_2$ (Supplementary Fig. 2), $WSe_2$ (Supplementary Fig. 3) and p-MSB (Supplementary Fig. 4), p-MSB-1/$WSe_2$ has much higher responsivity under the UV light, which can be evaluated by $R$ and $D^*$. The $R$ is calculated by $R = I_{ph}/SP_\lambda$,[36] where $S$ is the effective area and $P_\lambda$ is the light intensity. The $D^*$ signifies the smallest detectable signal, which is calculated by

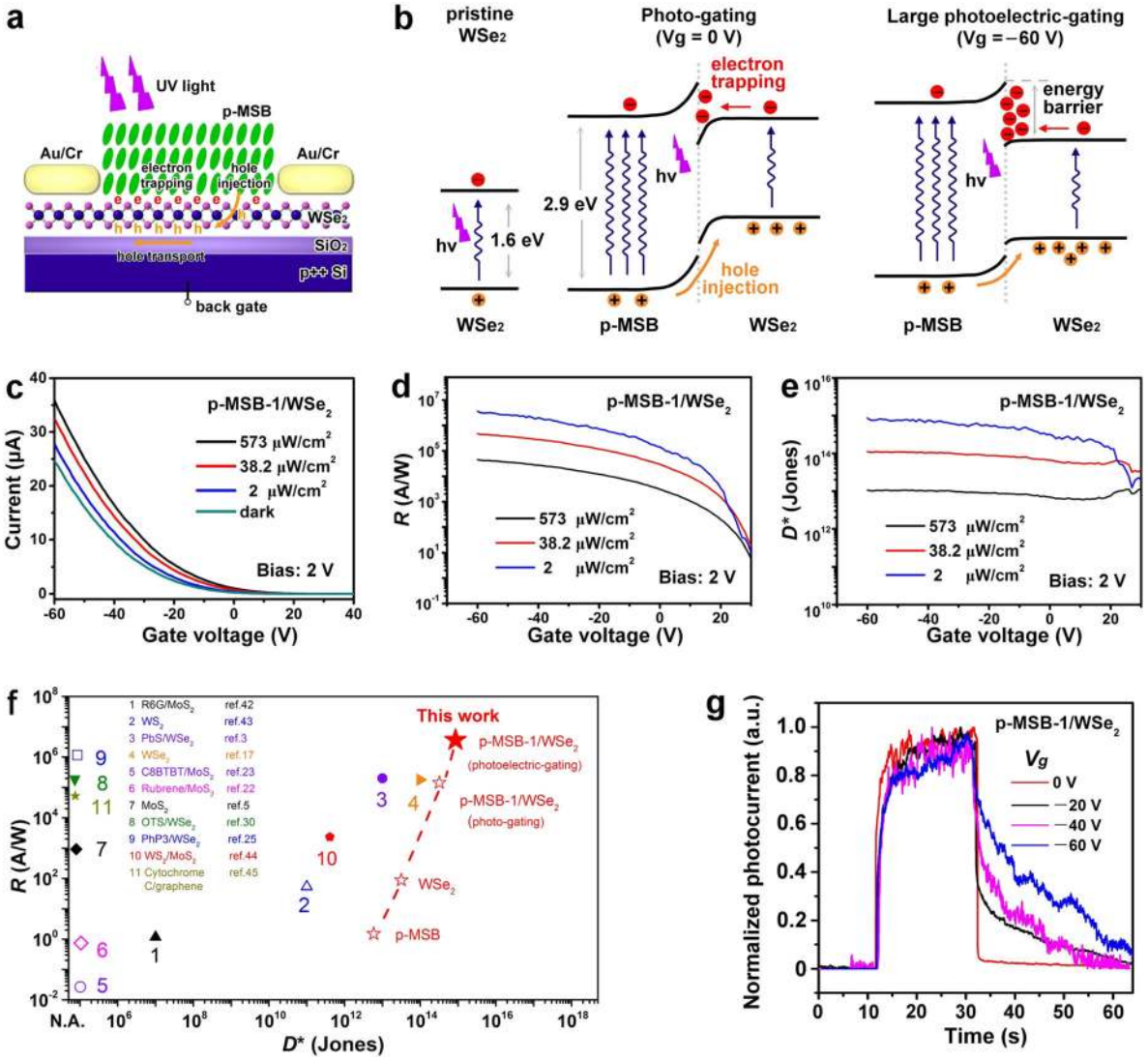


**Fig. 3** Photoresponse under large photoelectric-gating modulation (365 nm light). **a** Device configuration and photogenerated charges in the device under illumination. **b** Energy band structures of $WSe_2$ (left) and p-MSB-1/$WSe_2$ under illumination. Compared with normal photo-gating (middle), more electrons are trapped at the interface when photoelectric-gating effect dominates (right). **c** Transfer curves of the p-MSB-1/$WSe_2$ device under different incident intensities. **d** *R* and **e** *D** vs. gate voltage under different intensities (at a 2 V bias). **f** *R* and *D** in this work compared with some of the best reported results of TMDs-based photodetectors. **g** Response time vs. normalized photocurrent of p-MSB-1/$WSe_2$ at different gate voltages

$D^* = R(S/2eI_{dark})^{1/2}$. At a 2 V bias (Fig. 2c, d, Supplementary Fig. 8), *R* and *D** of p-MSB-1/$WSe_2$ are 1135 A/W and $10^{14}$ Jones under 365 nm light (10.7 μW/cm$^2$), and 987 A/W and $10^{13}$ Jones under 405 nm light (22.3 μW/cm$^2$), respectively. At a bias of 10 V (Fig. 2e, f), *R* and *D** of p-MSB-1/$WSe_2$ increase to $1.74 \times 10^4$ A/W and $10^{13}$ Jones under 365 nm light (3.6 μW/cm$^2$), and $3.27 \times 10^3$ A/W and $10^{13}$ Jones under 405 nm light (31.6 μW/cm$^2$). Under the same measurement condition, these values are about 1–2 or 3 orders of magnitude higher than that of pristine $WSe_2$ or p-MSB (Fig. 2c–f), respectively, and are about seven times higher than that of p-MSB-3/$WSe_2$, indicating the importance of the heterostructure and its morphology in achieving high photodetecting performance.

The high *R* and *D** of p-MSB-1/$WSe_2$ are attributed to the photo-gating modulation effect at the heterostructure (Fig. 3a, b). The highest occupied molecular orbital (HOMO) and lowest unoccupied molecular orbital (LUMO) of p-MSB are 5.6 and 2.7 eV, respectively.[37] The valence band maximum (VBM) and conduction band minimum (CBM) of monolayer $WSe_2$ are 5.10 and 3.53 eV, respectively.[38] Under illumination, p-MSB serves as a light absorber; most photoexcited carriers are generated in p-MSB due to the strong absorption of UV light (Supplementary Fig. 9). A built-in electric field across the junction separates the photoexcited electrons and holes. The HOMO of p-MSB is lower than the VBM of $WSe_2$, which allows the photoexcited holes transfer from p-MSB to $WSe_2$ and then transport in $WSe_2$ under a bias voltage. Owing to the high mobility, the $WSe_2$ serves as the main conduction channel. At the same time, a 0.83 eV electron-rejected barrier exists between LUMO of p-MSB and CBM of $WSe_2$, thus the photoexcited electrons in $WSe_2$ are trapped at the interface, resulting in unidirectional carrier injection from p-MSB to $WSe_2$.[39] The trapped electrons modulate the conduction of the $WSe_2$, introducing additional increase of photoresponsivity compared with normal photo-gating effect. As a result of the photo-gating modulation, p-MSB-1/$WSe_2$ has higher *R* and *D** compared with pristine p-MSB and $WSe_2$. The photo-gating effect usually leads to the shift of $V_{th}$ under illumination.[4] Fig. 3c shows that the $V_{th}$ shifts positively with the increasing incident power from 2 to 573 μW/cm$^2$, which is similar with other photo-gating

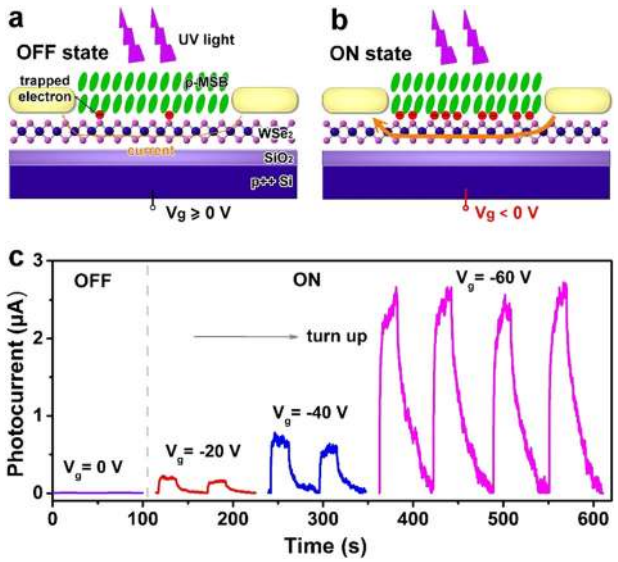


**Fig. 4** Electric-gating switchable photodetector. **a**, **b** Schematics of the device in "OFF" state and "ON" state, respectively. In **b**, under a negative gate voltage, more electrons are trapped at the interface, which leads to an increase of the photocurrent, corresponding to the "ON" state. **c** Photocurrent response (365 nm light) of the p-MSB-1/$WSe_2$ device under different gate voltages (bias voltage: 2 V)

TMDs-based photodetectors,[4,40,41] proving the photo-gating modulation in p-MSB-1/$WSe_2$. Moreover, the morphology of the interface is of great importance in this process. The high quality and large interface area of 2D epitaxial p-MSB-1/$WSe_2$ heterostructure prepared by PVD allows efficient charge transfer and trapping in photo-gating modulation, and results in higher photodetecting performance compared with p-MSB-3/$WSe_2$ (Fig. 2c, d, Supplementary Fig. 2).

### Large photoelectric-gating effect of p-MSB/$WSe_2$

The photodetecting performance of p-MSB-1/$WSe_2$ can be further improved by applying an electric gate ($V_g$). The ratio of current at light/dark as a function of gate bias is shown in Supplementary Fig. 10. The transfer curves, $R$ vs. $V_g$ and $D^*$ vs. $V_g$ under different incident power density, are shown in Fig. 3c–e, respectively. Under 2 μW/$cm^2$ 365 nm light, the $R$ ($V_{sd} = 2$ V) is $1.4 \times 10^5$ A/W when $V_g = 0$ V, and it increases up to $3.6 \times 10^6$ A/W by more than 5 orders when $V_g$ varies from 20 V to −60 V. This value is 7 orders of magnitude higher than other reported organic-TMDs heterostructures.[22,23] $D^*$ ($V_{sd} = 2$ V) reaches $2.5 \times 10^{14}$ Jones with the incident power density of 2 μW/$cm^2$. The value increases to $8.6 \times 10^{14}$ Jones when $V_g$ varies from 20 V to −60 V. Therefore, compared with the pristine TMDs or TMDs-based heterostructures (Fig. 3f),[42,43] although the $R$ and $D^*$ of p-MSB-1/$WSe_2$ are comparable or lower under photo-gating, the values dramatically increase by orders of magnitude to a level among one of the highest values for TMDs-based heterostructure, to the best of our knowledge, when a negative $V_g$ is applied.

Dramatic increase of photoresponse under a negative $V_g$ is attributed to a new type of photo-gating effect, called large photoelectric-gating effect. Unlike normal photo-gating or photoelectric-gating modulation, the p-MSB-1/$WSe_2$ has interfacial energy barrier between LUMO and CBM in band alignment, which allows unidirectional carrier injection. When a negative $V_g$ is applied, the Femi level of $WSe_2$ shifts downwards, leading to increase of the interfacial energy barrier. Thus, more and more photoexcited electrons are trapped at the interface, introducing dramatic increase of the photo-gating modulation. Therefore, as a result of the tunable energy barrier in p-MSB-1/$WSe_2$, the interfacial charge trapping processes are effectively modulated by the synergy of photo-gating and electric-gating effects, leading to increase of the $R$ and $D^*$ by several orders. This mechanism can be proved by the $V_g$ dependence of the response speed. The dynamic photoresponse of normalized photocurrent at different $V_g$ is shown in Fig. 3g. The rise and decay time of photocurrent are 120 and 80 ms when $V_g = 0$ V, about 1–2 orders of magnitude faster than that (rise time: 2 s, decay time: 25 s) when $V_g = -60$ V, which indicates that the electrical gating can effectively modulate the charge trapping process, and more electrons are accumulated when a negative $V_g$ is applied.[44,45]

### Electric-gating switchable photodetectors

As a result of electric-gating modulated charge trapping process (Fig. 4a, b), the photocurrent response of p-MSB-1/$WSe_2$ can be switched "ON" and "OFF", or turned up by applying different $V_g$. As shown in Fig. 4c, when alternating dark and light illumination (10.7 μW/$cm^2$, 365 nm), the p-MSB-1/$WSe_2$ photodetector exhibits a good reversible detecting behavior. At $V_g = 0$ V, the photocurrent response (at $V_{sd} = 2$ V) remains a low value down to 5.5 nA, corresponding to the "OFF" state. When applying a negative $V_g$, the large photoelectric-gating effect increases the photocurrent response by about 1–3 orders to 200 nA ($V_g = -20$ V), 700 nA ($V_g = -40$ V), 2.5 μA ($V_g = -60$ V), corresponding to the "ON" state. In the "ON" state, the photocurrent response increases with increasing negative $V_g$, implying that the photodetector can be turned up by applying a larger negative $V_g$.

## DISCUSSION

In this article, we find that sufficient supply of gas-phase molecules in PVD is pivotal to obtain high-quality 2D epitaxial van-der-Waals interface of p-MSB/$WSe_2$, which is of great importance for achieving high-performance photodetectors. This finding extends the understanding of controllable growth of organic crystals on TMDs, and will be valuable for the practical applications of organic/TMDs. More importantly, p-MSB/$WSe_2$ has an electric-gating tunable barrier at the interface, which allows effective modulation of the interfacial charge trapping process by $V_g$. Thus, as a result of the synergy of photo-gating and electric-gating effects, the performance can be dramatically improved by large photoelectric-gating modulation. At a $V_g$ of −60 V, $R$ and $D^*$ of p-MSB/$WSe_2$ increased to $3.6 \times 10^6$ A/W and $8.6 \times 10^{14}$ Jones by 25- and 3-folds, which are among the highest values for TMDs-based heterostructures, orders of magnitude higher than that of van-der-Waals heterostructures without interfacial electric-gating tunable barrier, i.e. graphene/$WSe_2$/graphene (0.1 A/W),[26] $WSe_2/MoS_2$ p–n junction (0.12 A/W),[27] etc. Besides p-MSB/$WSe_2$, this new strategy also has potential for application in heterostructures made of other materials, opening up promising avenues for designing photodetectors with higher performance. Moreover, we demonstrate an electric-gating switchable photodetector based on the large photoelectric-gating effect, which can be switched "ON" and "OFF" or be turned up by $V_g$, indicating the great potential of this strategy in developing new types of photoelectrical devices or applications.

## METHODS

### Epitaxial growth of p-MSB on $WSe_2$

Se powder (400 mg, 99.5%, Sigma-Aldrich) and $WO_3$ powder (40 mg, 99.9%, Sigma-Aldrich) were used as precursors for CVD growth of $WSe_2$ crystals. Five milligrams p-MSB (>98.0%) powder was placed in a quartz boat, locating in the center of the furnace. The p-MSB was purified at 190 °C for 1 h before epitaxial growth. $WSe_2$ crystals were placed downstream from the p-MSB source. The distance between $WSe_2$ and p-MSB source ranged from 12 to 14 cm. The furnace was heated to 180 °C, and then epitaxial growth took place at a low pressure of $3.1 \times 10^{-1}$ Torr (Ar) for 15–25 min. After growth, the furnace was cooled to room temperature in Ar.

### Characterization

The samples were measured by an optical microscope (Olympus), AFM (Multimode 8, Bruker, noncontact mode), Raman (XploRA, HORIBA JobinYvon, laser: 532 nm), and a ultraviolet and visible spectrophotometer (Lambda 750, Perkin-Elmer).

### Device fabrication and measurement

The drain and source electrodes (5 nm/50 nm Cr/Au) were patterned on the sample by e-beam lithography (FEI, NOVA NANOSEM450) and thermal evaporator (Kurt. J. Lesker, Nano 36). To obtain a better contact between the sample and the Au/Cr electrodes, the devices were annealed in vacuum at 250 °C for 90 min. Electrical measurements were conducted in ambient using a semiconductor analyzer (Keysight, B1500A) and a probe station (Everbeing, PE-4).

### Data availability

Data that support the findings of this study are available from the corresponding authors upon reasonable request.

## ACKNOWLEDGEMENTS

This work was supported by National Program for Thousand Young Talents of China, the National Natural Science Foundation of China (51773041, 21544001, 21603038), Shanghai Committee of Science and Technology in China (Grant No. 18ZR1404900), State Key Laboratory of Molecular Engineering of Polymers and Fudan University.

## AUTHOR CONTRIBUTIONS

D.W. designed research and supervised the project. Z.C. prepared the sample and did AFM, Raman, UV measurement. Z.C. and M.C. did device measurement. J.Z. and Y.Y. prepared the WSe2. X.C. did thermal deposition. D.W. and Z.C. prepared the manuscript. All authors commented on the manuscript.

## ADDITIONAL INFORMATION

**Supplementary information** accompanies the paper on the *npj 2D Materials and Applications* website (https://doi.org/10.1038/s41699-018-0066-2).

**Competing interests:** The authors declare no competing interests.

**Publisher's note:** Springer Nature remains neutral with regard to jurisdictional claims in published maps and institutional affiliations.

## REFERENCES

1. Konstantatos, G. et al. Hybrid graphene–quantum dot phototransistors with ultrahigh gain. *Nat. Nanotechnol.* **7**, 363–368 (2012).
2. Sun, Z. et al. Infrared photodetectors based on CVD-grown graphene and pbs quantum dots with ultrahigh responsivity. *Adv. Mater.* **24**, 5878 (2012).
3. Hu, C. et al. Synergistic effect of hybrid PbS quantum dots/2D-$WSe_2$ toward high performance and broadband phototransistors. *Adv. Funct. Mater.* **27**, 1603605 (2017).
4. Furchi, M. M., Polyushkin, D. K., Pospischil, A. & Mueller, T. Mechanisms of photoconductivity in atomically thin $MoS_2$. *Nano Lett.* **14**, 6165–6170 (2014).
5. Lopez-Sanchez, O., Lembke, D., Kayci, M., Radenovic, A. & Kis, A. Ultrasensitive photodetectors based on monolayer $MoS_2$. *Nat. Nanotechnol.* **8**, 497–501 (2013).
6. Lee, H. S. et al. $MoS_2$ nanosheet phototransistors with thickness-modulated optical energy gap. *Nano Lett.* **12**, 3695–3700 (2012).
7. Choi, W. et al. High-detectivity multilayer $MoS_2$ phototransistors with spectral response from ultraviolet to infrared. *Adv. Mater.* **24**, 5832–5836 (2012).
8. Mak, K. F., Lee, C. & Hone, J. A new direct-gap semiconductor. *Phys. Rev. Lett.* **105**, 136805 (2010).
9. Splendiani, A., Sun, L. & Zhang, Y. Emerging photoluminescence in monolayer $MoS_2$. *Nano Lett.* **10**, 1271–1275 (2010).
10. Radisavljevic, B. et al. Single-layer $MoS_2$ transistors. *Nat. Nanotechnol.* **6**, 147–150 (2011).
11. Wang, H. et al. Integrated circuits based on bilayer $MoS_2$ transistors. *Nano Lett.* **12**, 4674–4680 (2012).
12. Kim, S. et al. High-mobility and low-power thin-film transistors based on multilayer $MoS_2$ crystals. *Nat. Commun.* **3**, 1011 (2012).
13. Nair, R. R. et al. Fine structure constant defines visual transparency of graphene. *Science* **320**, 1308–1308 (2008).
14. Xia, F. et al. Photocurrent imaging and efficient photon detection in a graphene transistor. *Nano Lett.* **9**, 1039–1044 (2009).
15. Britnell, L. et al. Strong light-matter interactions in heterostructures of atomically thin films. *Science* **340**, 1311–1314 (2013).
16. Peng, B., Ang, P. K. & Loh, K. P. Two-dimensional dichalcogenides for light-harvesting applications. *Nano Today* **10**, 128–137 (2015).
17. Zhang, W. et al. Role of metal contacts in high-performance phototransistors based on $WSe_2$ monolayers. *ACS Nano* **8**, 8653–8661 (2014).
18. Eda, G. & Maier, S. A. Two-dimensional crystals: managing light for optoelectronics. *ACS Nano* **7**, 5660–5665 (2013).
19. Kufer, D. et al. Hybrid 2D-0D $MoS_2$-PbS quantum dot photodetectors. *Adv. Mater.* **27**, 176–180 (2015).
20. Dong, H., Zhu, H., Meng, Q., Gong, X. & Hu, W. P. Organic photoresponse materials and devices. *Chem. Soc. Rev.* **41**, 1754–1808 (2012).
21. Wang, C., Dong, H., Hu, W., Liu, Y. & Zhu, D. Semiconducting π-conjugated systems in field-effect transistors: a material Odyssey of organic electronics. *Chem. Rev.* **112**, 2208–2267 (2011).
22. Liu, F. C. et al. Van Der Waals p-n junction based on an organic-inorganic heterostructure. *Adv. Funct. Mater.* **25**, 5865–5871 (2015).
23. He, D. Y. et al. A Van Der Waals p-n heterojunction with organic/inorganic semiconductors. *Appl. Phys. Lett.* **107**, 183103 (2015).
24. Liu, X. L. et al. Epitaxial ultrathin organic crystals on graphene for high-efficiency phototransistors. *Adv. Mater.* **28**, 5200–5205 (2016).
25. Jo, S. H. et al. A high-performance $WSe_2$/h-BN photodetector using a triphenylphosphine ($PPh_3$)-based n-doping technique. *Adv. Mater.* **28**, 4824–4831 (2016).
26. Massicotte, M. et al. Picosecond photoresponse in Van Der Waals heterostructures. *Nat. Nanotechnol.* **11**, 42–46 (2016).
27. Lee, C. H. et al. Atomically thin p-n junctions with Van Der Waals heterointerfaces. *Nat. Nanotechnol.* **9**, 676–681 (2014).
28. Bie, Y. Q. et al. A $MoTe_2$-based light-emitting diode and photodetector for silicon photonic integrated circuits. *Nat. Nanotechnol.* **12**, 1124–1129 (2017).
29. Yang, J. et al. Improved growth behavior of atomic-layer-deposited high-k dielectrics on multilayer $MoS_2$ by oxygen plasma pretreatment. *ACS Appl. Mater. Interfaces* **5**, 4739–4744 (2013).
30. Kang, D. H. et al. High-performance transition metal dichalcogenide photodetectors enhanced by self-assembled monolayer doping. *Adv. Funct. Mater.* **25**, 4219–4227 (2015).
31. Kang, D. H. et al. Controllable nondegenerate p-type doping of tungsten diselenide by octadecyltrichlorosilane. *ACS Nano* **9**, 1099–1107 (2015).
32. Li, R. J. et al. Gibbs-Curie-Wulff theorem in organic materials: a case study on the relationship between surface energy and crystal growth. *Adv. Mater.* **28**, 1697–1702 (2012).
33. Yang, J. et al. High-quality large-size organic crystals prepared by improved physical vapor growth technique and their optical gain properties. *J. Phys. Chem. C.* **115**, 9171–9175 (2011).
34. Joshi, N. V. *Photoconductivity: Art, Science, and Technology* (Marcel Dekker, New York, 1990).
35. Kind, H. et al. Nanowire ultraviolet photodetectors and optical switches. *Adv. Mater.* **14**, 158 (2002).
36. Koppens, F. H. L. et al. Photodetectors based on graphene, other two-dimensional materials and hybrid systems. *Nat. Nanotechnol.* **9**, 780–793 (2014).
37. Nakanotani, H. et al. Blue-light-emitting ambipolar field-effect transistors using an organic single crystal of 1,4-bis (4-methylstyryl) benzene. *Appl. Phys. Express* **1**, 091801 (2008).
38. Zhou, C. et al. Carrier type control of $WSe_2$ field-effect transistors by thickness modulation and $MoO_3$ layer doping. *Adv. Funct. Mater.* **26**, 4223 (2016).
39. Qian, C. et al. Organic phototransistors: high-performance organic heterojunction phototransistors based on highly ordered copper phthalocyanine/para-sexiphenyl thin films. *Adv. Funct. Mater.* **27**, 1604933 (2017).
40. Kufer, D. & Konstantatos, G. Highly sensitive, encapsulated $MoS_2$ photodetector with gate controllable gain and speed. *Nano Lett.* **15**, 7307–7313 (2015).
41. Octon, T. J. et al. Fast high-responsivity few-layer $MoTe_2$ photodetectors. *Adv. Opt. Mater.* **4**, 1750–1754 (2016).
42. Yu, S. H. et al. Dye-sensitized $MoS_2$ photodetector with enhanced spectral photoresponse. *ACS Nano* **8**, 8285–8291 (2014).
43. Zeng, L. H. et al. High-responsivity UV-vis photodetector based on transferable $WS_2$ film deposited by magnetron sputtering. *Sci. Rep.* **6**, 20343 (2016).
44. Tan, H. et al. Lateral graphene-contacted vertically stacked $WS_2$/$MoS_2$ hybrid photodetectors with large gain. *Adv. Mater.* **29**, 1702917 (2017).
45. Gong, M. et al. Polarity-controlled attachment of cytochrome C for high-performance cytochrome C/graphene Van Der Waals heterojunction photodetectors. *Adv. Funct. Mater.* **28**, 1704797 (2018).